UNIVERSITY OF ZÜRICH

Avalanche Photodiode (APD) Testing in Liquid Xenon

by

Michael Miloradovic

Bachelor thesis in physics
supervised by Prof. Laura Baudis and Martin Auger

Physics Institute UZH
Faculty of Science

November 2013

Acknowledgements

I would like to thank Prof. Laura Baudis, my supervisor Martin Auger, and the whole group for helping me with this experiment and for the inspiring atmosphere in the laboratory.

Contents

List of Figures

Chapter 1

Introduction

There seems to be more to our universe than meets the eye. All the stars, star formations, and gas clouds make up only 15% of the matter in the universe. The remaining 85% is invisible non-baryonic matter called Dark Matter [1].

Over the course of the last and continuing into the new century, a substantial amount of evidence has been gathered in support of this theory (See Section 1.1). Phenomena have been observed that seem best explained by a large quantity of missing mass, big bang nucleosynthesis processes cannot account for [2]. But so far, Dark Matter has eluded all forms of direct detection [3]. In an effort to change that, a great variety of astroparticle physics detectors have been constructed across the globe.

The XENON experiment is located in the Gran Sasso underground laboratory in Italy. It uses liquid xenon detection techniques wherein Dark Matter induced scintillation light emitted by the decay of excited molecular xenon states after elastic scattering off the liquid xenon nuclei could directly prove the existence of Dark Matter [4].

One of the key factors is the use of high-sensitivity light detectors: photomultiplier tubes (PMTs). They traditionally serve to fulfill this role but, in turn, introduce additional radiation into the system due to their size and mass [5]. Smaller detectors such as Avalanche Photodiodes (APDs) could be the next generation of high-sensitivity photodetectors [6].

This thesis will thus concentrate on the testing of APDs in the framework of Dark Matter detection.

The results of the measurements will then be compared in the discussion (See Chapter 5) to those of existing literature of Ludhova et al. 2005 [7], an experiment performed at the Paul Scherrer Institute (PSI) in Switzerland, and Shagin et al. 2009 [6] at Rice University, USA.

1.1 Evidence for Dark Matter

The need for a large quantity of invisible matter was first introduced in the study of galaxy and galaxy cluster motion [8]. New technology in the 1970s allowed for the measurement of highly accurate galaxy rotation curves. They clearly showed the velocity of stars outside the main bulk remaining constant even to the outer reaches of a spiral galaxy [9]. The mass distribution of a galaxy is therefore not coherent with the distribution of its stars.

In 2006, data from the Hubble Space Telescope (HST) for the visible spectrum, the Chandra X-ray Observatory, and weak gravitational lensing was used to create a map of the galaxy cluster 1E 0657–558 as seen in Figure 1.1. It shows a galaxy cluster collision, apparent due to the bow shock experienced by the galaxy clusters' plasma; hence often referred to as the "Bullet Cluster". The low star density in a cluster, on the other hand, allows them to simply pass through each other. The corresponding plasma is, on average, ten times as heavy as all the stars in a cluster combined. However, a clear separation of the plasma and the centers of potential, determined by weak gravitational lensing, is visible. Dark Matter in form of Weakly Interacting Massive Particles (WIMPs) could make up most of the mass of a galaxy cluster. Unaffected by the galaxy cluster collision due to being only weakly interacting, the Dark Matter still resides inside the clusters and thus bends the light more significantly than the plasma. [10]

The local Dark Matter density can be simulated by different Dark Matter distribution models. Equation 1.1 shows the range of current simulated values of the local Dark Matter density [11]:

$$p_{\odot} = 0.2 - 0.4\,\mathrm{GeV}\,cm^{-3} \tag{1.1}$$

Direct Dark Matter detection experiments can make use of these local Dark Matter density simulations to derive cross sections of WIMP Dark Matter.

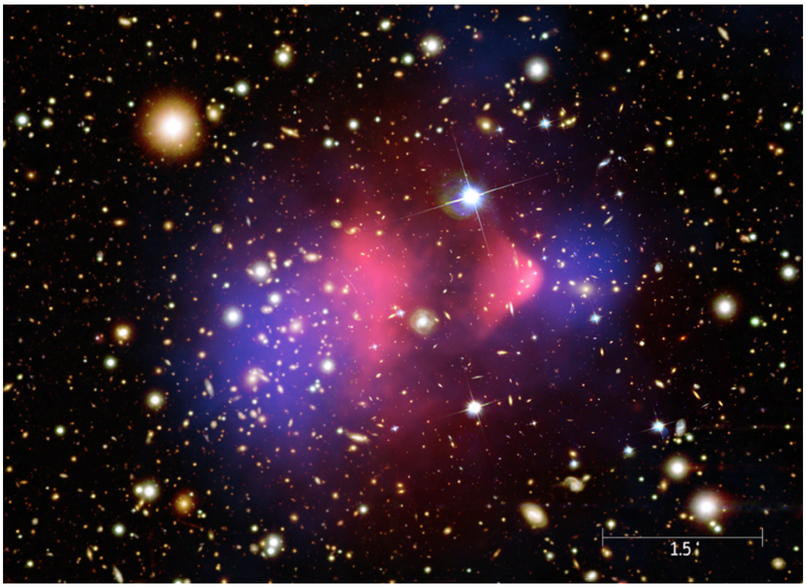

FIGURE 1.1: Overlay of the Chandra X-ray Observatory (pink), weak gravitational lensing (purple), and Hubble Space Telescope (HST) pictures of 1E 0657–558. The plasma seen by X-ray (pink) is separated from the centers of potential (purple), which can only be explained by the existence of Dark Matter. Figure from [12].

1.2 The XENON Dark Matter Project

The XENON Dark Matter Project uses liquid noble gas detection methods with liquid xenon as a target. Xenon is an excellent scintillator with high light yields, while being intrinsically clean from any radioactive contaminations [13]. Another advantage is the scalability to larger quantities of xenon for future experiments such as XENON1T, allowing for even greater sensitivity on the spin-independent WIMP-nucleon cross-section [14] (See Figure 1.3 for current limits). Located in the Laboratori Nazionali del Gran Sasso (LNGS) in Italy, the mountain above the underground laboratory shields the experiment from cosmic background radiation. Dark Matter particles in the form of Weakly Interacting Massive Particles (WIMPs) pass directly through the rock, reaching into the liquid xenon target (See Figure 1.2). Elastic scattering off the liquid xenon nuclei leads to the excitation and ionisation of xenon atoms and in combination with neutral atoms to excimer xenon states. The decay of these states produces scintillation light, the ionisation free electrons. Drawn by an electric field into the gas phase of the xenon at the top of the container, the free electrons create another flash of light, which can then be detected again and compared to the initial one, revealing the type of particle that caused the interaction. [4]

Even though photomultiplier tubes (PMTs), the photodetectors used in XENON10 and XENON100, are a reliable and mature technology, they have an intrinsic problem. Due to their size, they introduce additional background radiation into the experiment, which

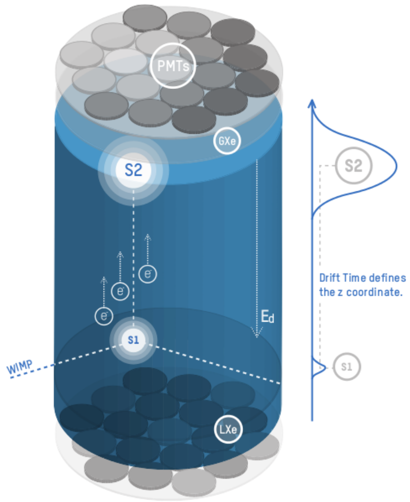

FIGURE 1.2: A Weakly Interacting Massive Particle (WIMP) enters liquid xenon chamber (LXe), interacts with xenon nucleus at S1 creating scintillation light and free electrons. These drift into gas phase xenon (GXe) emitting another flash of light at S2 also detected by photomultipliers (PMTs). Figure from [15].

ultimately limits the degree of sensitivity that can be achieved [5]. Avalanche Photodiodes (APDs), however, are very compact (See Chapter 2) and have low associated radiation. They could thus benefit not only Dark Matter detection, but also other high purity experiments, such as the ultra-low background search for neutrinoless double-beta decay that could prove that the neutrino is a majorana particle [16].

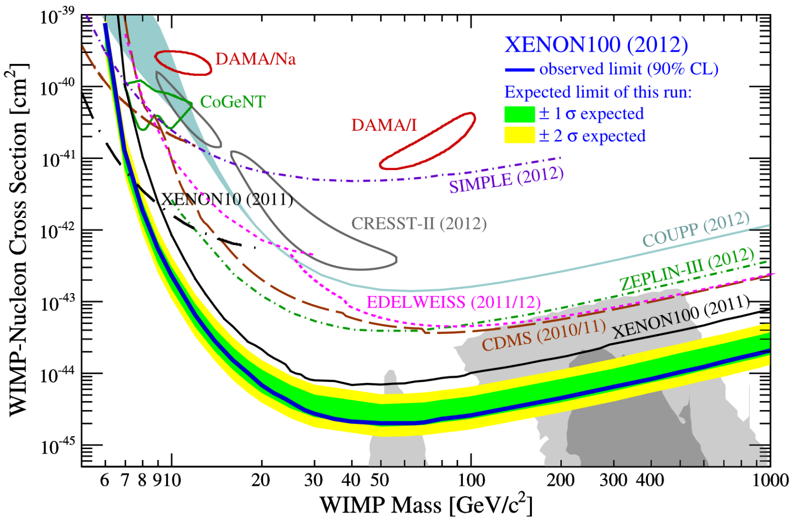

FIGURE 1.3: Limits on WIMP-nucleon interaction cross-section related to mass from indicated experiments such as XENON10 and XENON100. Figure from [3].

Chapter 2

APDs - Avalanche Photodiodes

APDs are high-speed, high-sensitivity silicon photodiodes that make use of the photoelectric effect to convert incoming photons into photoelectrons [17]. These are in turn multiplied through an internal avalanching process in order to amplify the outgoing electron signal [18]. This gain mechanism can create a stronger signal out of very faint light and is thus ideal for high sensitivity measurements [17, 18]. Making use of these effects inside a solid body gives the advantage of very compact APDs and thus low associated radioactivity due to the small size and mass [6].

2.1 Avalanching Mechanism

Illuminated by light with energy above the band gap energy of the silicon photodiode, electron-hole pairs are created inside the APD as the valence band electrons are excited to move into the conduction band [18] (See Figure 2.1). The ratio of electron-hole pairs generated to incoming photons is called *quantum efficiency* [6].

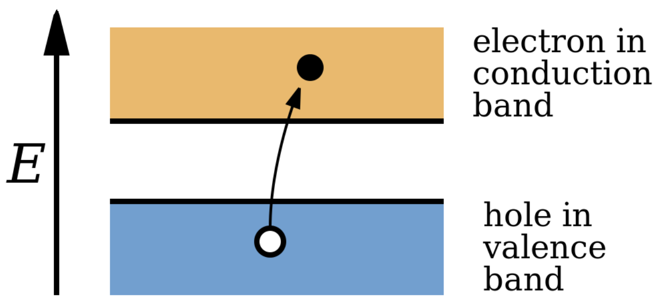

FIGURE 2.1: Schematic diagram of valence and conduction bands of a semiconductor. Exposed to light, valence band electrons are excited to move into conduction band.

Applying a reverse high voltage on the APD forces the electrons and holes to drift in opposite directions of the applied field (See Figure 2.2). The strength of the field determines the drift speed: Equation 2.1 shows the drift speed (v) in relation to the charge carrier mobility (μ), applied reverse high voltage (V), and the thickness of the APD (d). Increasing the reverse high voltage leads to higher energy build-ups of drifting electrons and holes that have not yet collided. In collisions with crystal lattices, new electron-hole pairs are formed, which in turn will be accelerated leading to further collisions. This chain reaction of electron-hole pair creations is called the *avalanching process*. The multiplication ratio is called *gain*. [17]

$$v = \mu \cdot \frac{V}{d} \tag{2.1}$$

The initial photocurrent amplification in this process starts to take place above a certain applied high voltage threshold referred to as *unity gain*. At unity gain, no multiplication is taking place, the drifting electrons and holes are just below the threshold of having enough energy to create further pairs [17].

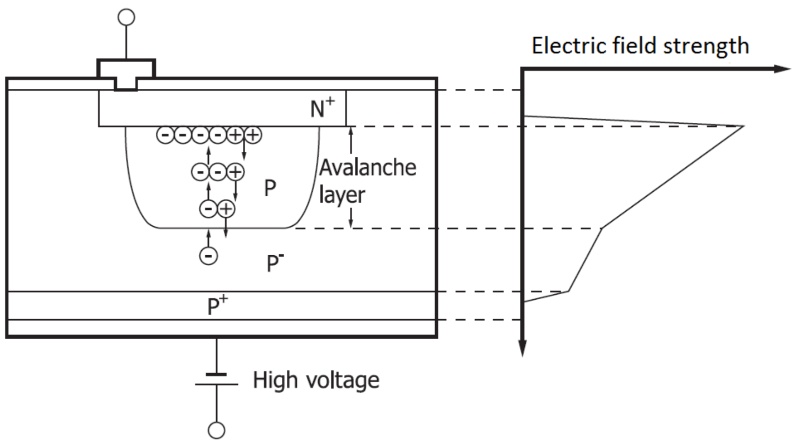

FIGURE 2.2: Schematic diagram of the APD avalanching mechanism. The reverse high voltage creates an electron and hole drift towards opposite sides. Figure from [18].

The APD gain is not only dependent on high voltage, but also on the temperature of the silicon. At high temperatures, the increased vibrations of the crystal lattices make collisions with electron-hole pairs more likely, keeping them from building up enough energy before a collision happens to create a new electron-hole pair [17]. The avalanching process is hindered. It is important to keep the temperature constant to allow for unchanged APD gain throughout a measurement. Lowest tested temperatures of various manufacturers stay at around 243–253 K [7, 17, 18] as the usual applications do not require lower temperatures, so the performance when operating at liquid xenon temperature is an important one to study.

2.2 Excess Noise Factor

For constant high voltage, the APD gain remains the mean value of each carrier's multiplication. On the other hand, there is statistical variation in the ionisation rate. Statistical noise, called *excess noise factor*, is introduced due to the stochastic nature of the avalanching process [18]. The signal-to-noise ratio worsens with a larger excess noise factor. The excess noise is expected to increase with higher multiplication ratios of the APD. Higher APD gain should thus increase the excess noise factor, which has been shown by tests at normal usage temperatures [7, 18]. This is another attribute that needs closer study for much lower temperatures than is usually accounted for. The excess noise factor (F) can be expressed by the electron-to-hole ionisation ratio (k) and gain (M), shown in Equation 2.2 [18]:

$$F = M \cdot k + (2 - \frac{1}{M})(1 - k) \tag{2.2}$$

Chapter 3

Experimental Setup

The two APDs of type RMD LAAPD S1315-P that are used in this experiment are flat silicon semiconductors with a 13.5 $mm \times 13.5$ mm sensitive area surrounded by 1 mm wide inactive material border [7] (See Figure 3.1).

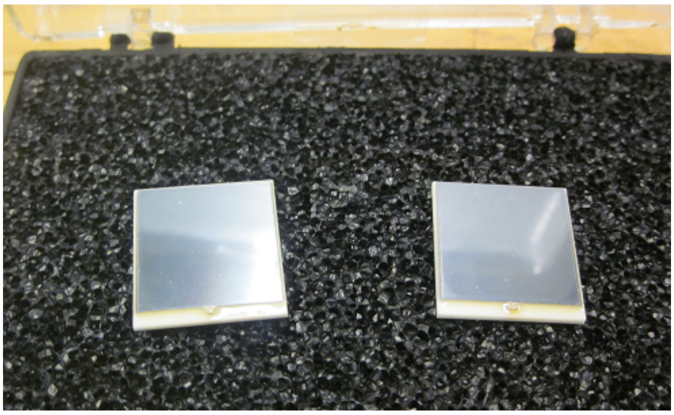

FIGURE 3.1: A close-up of the two Avalanche Photodiodes (APDs) of type RMD LAAPD S1315-P used in this experiment. Dimensions: 13.5 $mm \times 13.5$ mm sensitive area, 1 mm wide inactive border.

They are to be immersed in 400 g liquid xenon (LXe). To keep them in place, a holder construction has been made consisting of two tight fit co-axial cylinders made of teflon. A high degree of light reflectivity make teflon an ideal holder material [19].

The outer teflon cylinder has two windows of the size of the APDs where they are positioned slightly lowered-in, facing outwards (See Figure 3.2). While the top side is open to allow sliding in the inner cylinder fixing the APDs in place. The delicate pins of the APDs can then be accessed through a diametral slit on the inner cylinder's bottom (See Figure 3.3). These pins carry the high voltage and the APD signal.

FIGURE 3.2: Outer teflon cylinder viewed from the inside (left). And with APDs in place, facing away and showing their pins (right).

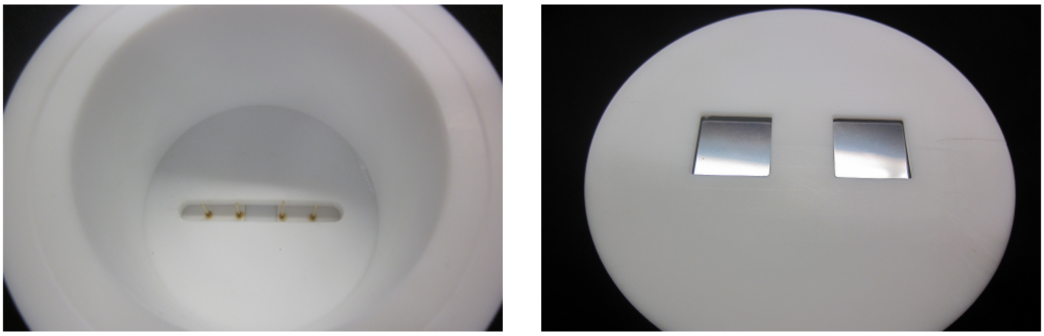

FIGURE 3.3: Inner teflon cylinder inside outer one, holding APDs in place (left). Turned upside down, the sensitive area of the APDs is visible (right).

The two-teflon-cylinder construct, containing the APDs facing outward, is then mounted onto a base leaving room for the xenon between the bottom of the base and the APDs. Small radial holes in the teflon base contain two PT-100 temperature sensors and a blue light LED. The hole for the LED does not quite reach into the base, and thus emits its light through a thin layer of teflon, which makes the light diffuse [19].

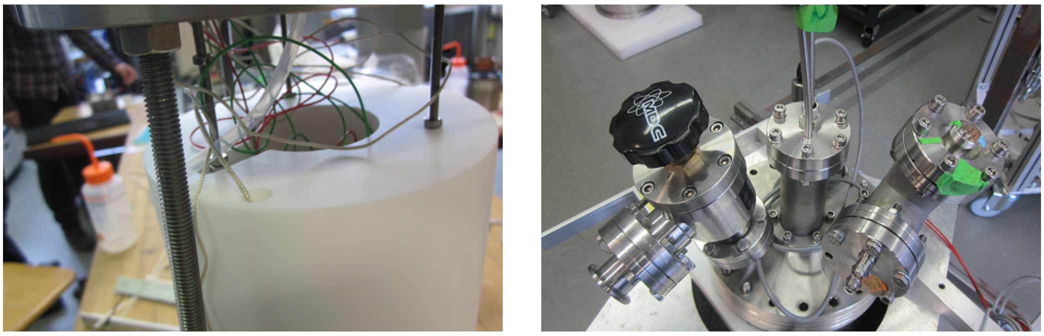

FIGURE 3.4: Mounted onto the vacuum seal (left) with APD signal (green/red), PT-100 (white), and LED wiring (white). Vacuum seal mounted onto chamber (right) showing black MDC chamber valve, LED port marked in orange, and temperature controller pins (green/blue).

The whole teflon construct is screwed onto the vacuum chamber seal (See Figure 3.4). The chamber is pumped to vacuum pressure before being cooled and filled with liquid xenon. The pumping process makes sure that a minimum of other elements, such as oxygen and water, remain inside. The chamber is already outfitted with a pressure sensor. The cabling of the APDs and the LED are soldered onto two different coaxial ports, while the temperature sensors are soldered onto multipin feed-through connectors. This way, they are connected to the outside of the chamber.

3.1 Signal Circuit

The blue LED is being controlled by the BNC 505 pulse generator through short voltage bursts. The APD signal and high voltage cabling are guided through a coaxial cable into the Canberra 2006 PreAMP, which in turn receives the high voltage from a HV supply in the laboratory and sends the APD signal pre-amplified into the ORTEC 671 amplifier. After signal shaping, the signal goes into either the ADC CAEN Mod. V1724 or the MCA CAEN N957, depending on the measurement. In the MCA measurements, the SpecAMP CAEN N968 has been used as an amplifier and the TTi TG 4001 as a pulse generator for the LED. A graphical representation of the circuit can be seen in Figure 3.5.

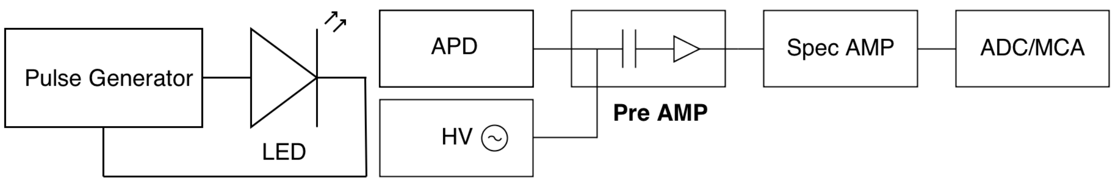

FIGURE 3.5: Signal circuit diagram.

3.2 Amplifier and MCA Calibration

Amplifier calibration is necessary to be able to recalculate signal strength when switching between the discrete gain settings ($\times 5$–$\times 1000$) on the ORTEC 671 (See Section 4.4 and 4.5). In the calibrations, the BNC 505 is directly fed into the amplifier. The slopes of each gain setting of the amplifier can be seen in Figure 3.6 on the bottom left.

Calibrating the MCA gives the ability to locate the zero point in MCA bins (See Figure 3.6, bottom right), so one can correctly understand the MCA behaviour of signal (See Section 4.5) and peaks detected when looking for scintillation light of a radioactive source.

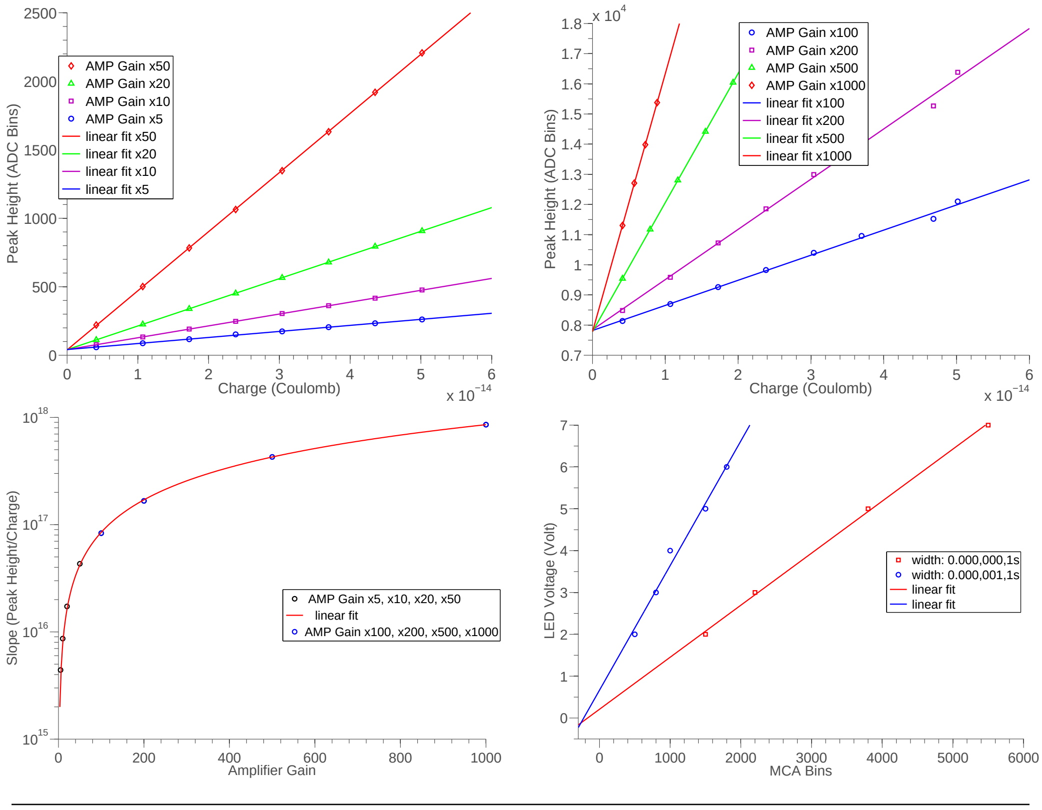

FIGURE 3.6: Calibration of the ORTEC 671 Amplifier over the full range of discrete gain settings ×5–×1000 (top). All the gain setting slopes (bottom, left). Calibration and zero point location of the MCA (bottom, right).

3.3 Temperature Control

The PT-100 temperature sensors change their resistance proportionally to their temperature. Connected to a temperature controller, the resistance can be measured and the temperature calculated (See Figure 3.7). An additional temperature sensor is positioned on the outside of the vacuum chamber at its bottom.

The sealed vacuum chamber is mounted inside a container that can be filled by opening an access valve to a liquid nitrogen dewar. A vacuum is created in the vacuum chamber and afterwards filled with purified xenon gas. The liquid nitrogen acting as a coolant is at 90 K, whereas the inside temperature goal for the xenon to become liquid is at 170 K. A circuit logic, as seen in Figure 3.8, is established to keep the liquid nitrogen height in the container at optimal level. At 1.7 bar, the pressure sensor closes a relay to a fill-height controller that has two fill-height sensors. If the sensors register the liquid nitrogen height in the container to be too low, the controller opens the valve to the liquid nitrogen dewar. The valve is closed as soon as both sensors are immersed in the liquid. The temperature controller has access to both the inside and the outside temperature sensors, as well as a heating unit on the outside of the vacuum chamber. Calculation

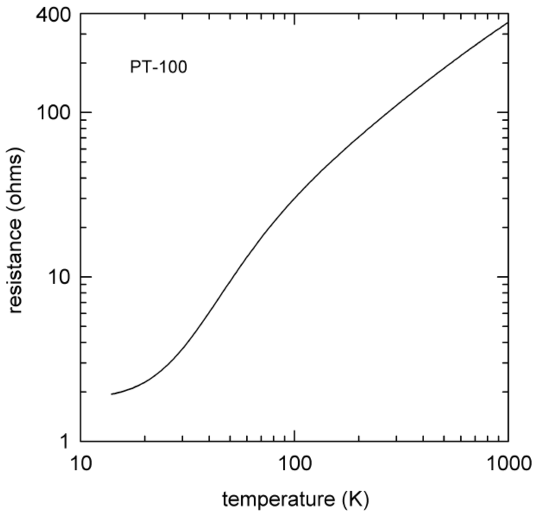

FIGURE 3.7: PT-100 calibration curve showing the proportional dependence of the platinum sensor's resistance to temperature in the region of interest between 100–200 K.

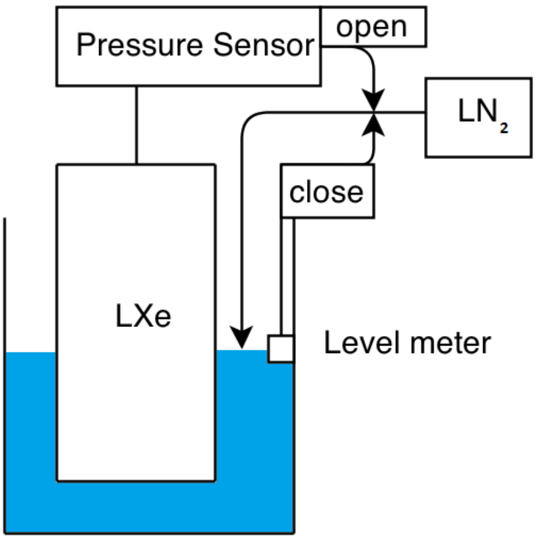

FIGURE 3.8: Schematic of the temperature control system showing the vacuum chamber filled with liquid xenon (LXe) cooled by the surrounding liquid nitrogen (blue). The pressure sensor and level meter sensors control the valve of the liquid nitrogen container (LN_2) used for refilling.

of the optimal heating curve allows the inside system to stay within 1 K temperature variance at 170 K with 1.5–1.7 bar pressure, as seen in Figure 3.9. For these values, the phase diagram (Figure 3.10) shows the xenon to be in liquid form.

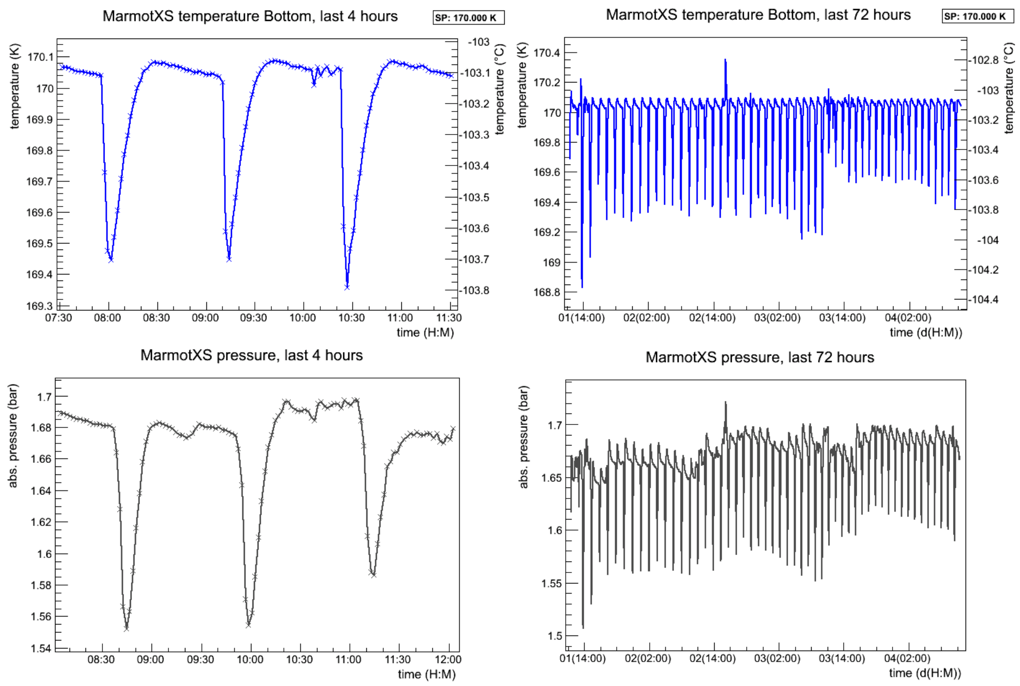

FIGURE 3.9: Inner temperature sensor history with temperature control in place over 4 hours (top left) and 72 hours (top right). Corresponding pressure sensor history over 4 hours (bottom left) and 72 hours (bottom right).

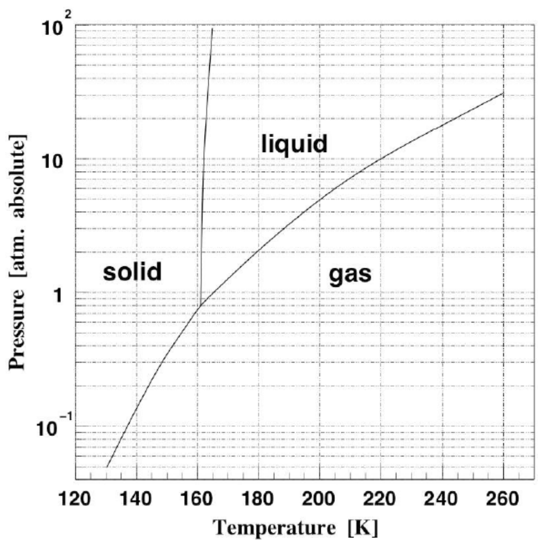

FIGURE 3.10: Phase diagram of xenon. Figure from [20].

Chapter 4

Measurements and Results

The measurements consist of tests on two APDs of the type RMD S1315-P in xenon gas at room temperature, 188 K, and finally liquid xenon at 170 K.

The starting graphs depict slight gain differences between the two APDs of same type. It is not the goal of this thesis to compare two identically built products, thus later graphs omit a comparison between the two APDs, as for example the logarithmic APD gain curves look identical.

To generate a signal from the APDs, they are exposed to diffuse light emitted by the blue LED inside the inner teflon cylinder [19]. The voltage bursts are kept in the 100 ns - 200 ms range as to limit the photon quantity produced.

4.1 APD Signal Comparison

In Figure 4.1, it is apparent that both APDs create a noticeable signal peak if the LED is emitting light. The LED emits bursts at 2.8 V with 200 ms width, while the APDs are on a high voltage of 1500 V. The background shows the measured noise created by the APDs if the LED is disabled.

Comparing both signals, one can see that even though the two APDs are of the same manufacturing type, they show a difference in amplitude. This could be due to dissimilar exposure to the diffuse light, but more likely a difference in gain. Each silicon chip produced is not perfectly equal to the next, so the individual avalanching process could vary between chips depending on purity and quantity of crystal defects, ultimately resulting in higher or lower gain [21].

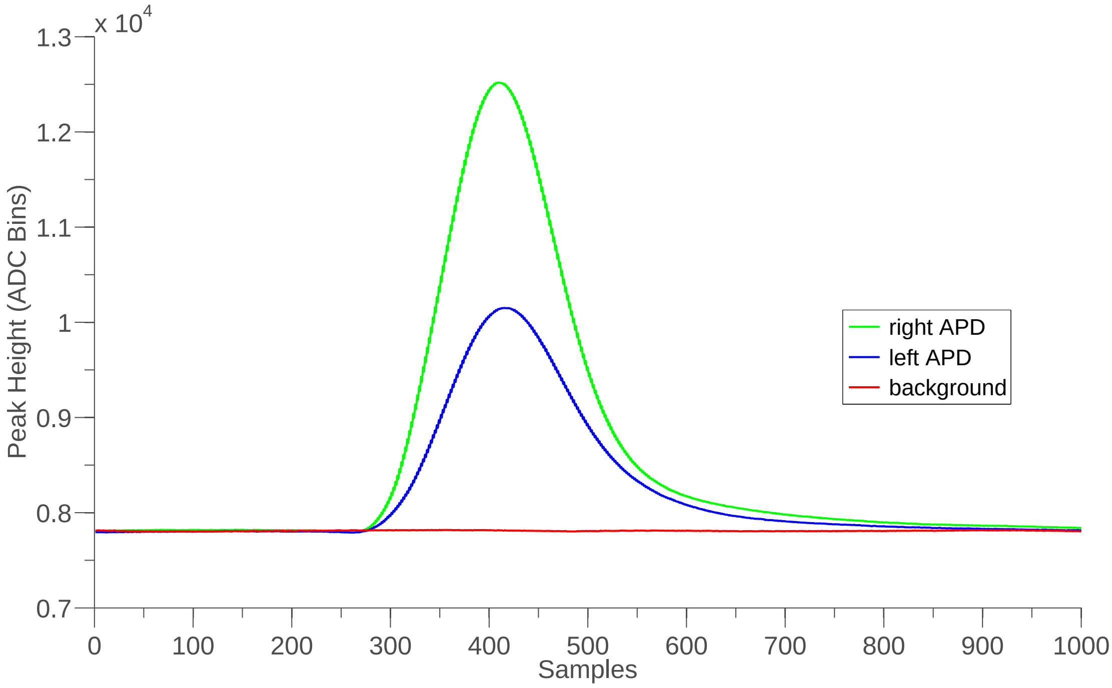

FIGURE 4.1: Signal of the right APD (green) measured at 1500 V high voltage and 2.8 V LED voltage, in comparison to the left APD (blue), and the background with disabled LED (red).

4.2 Variation of High Voltage and LED Voltage

It is interesting to see what happens if the voltage on the LED and the high voltage on the APD are increased (See Figure 4.2). The former produces a higher quantity of photons emitted that create photoelectrons inside the APDs, which in turn are being multiplied by the APD gain factor through the avalanching process. The latter raises the APD gain factor, so both ultimately increase the signal strength.

For a constant amount of photoelectrons, increasing the high voltage on the APDs boosts the signal significantly. The width of the LED Voltage bursts is 1 ms.

A histogram of this data shows how the peaks shift to the right for a stronger signal (See Figure 4.3). It also reveals how higher voltage on the LED increases the peak-to-peak distance for the different high voltage peaks. Whereas the leftmost peak is the sum of the four 4.10 V peaks bunched together, the four peaks of the 4.15 V measurement are clearly distinguishable. Looking at these four peaks, a visible broadening of the gaussians is observed the more the high voltage is increased.

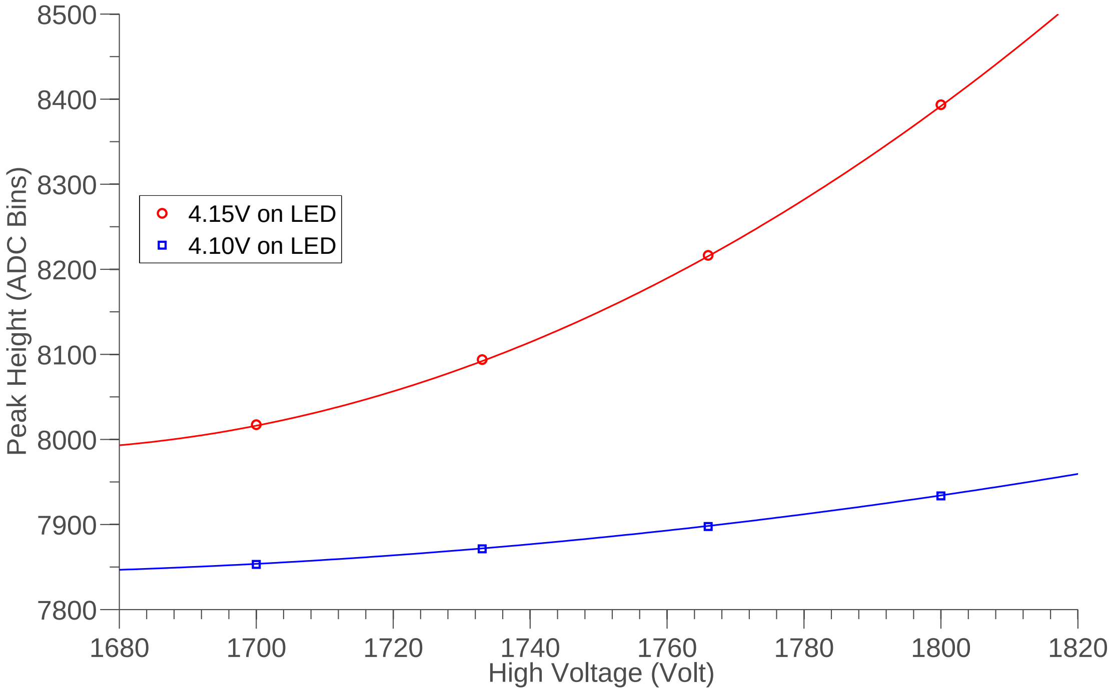

FIGURE 4.2: Signal behaviour with rising high voltage for 4.10 V LED voltage (blue) and 4.15 V LED voltage (red).

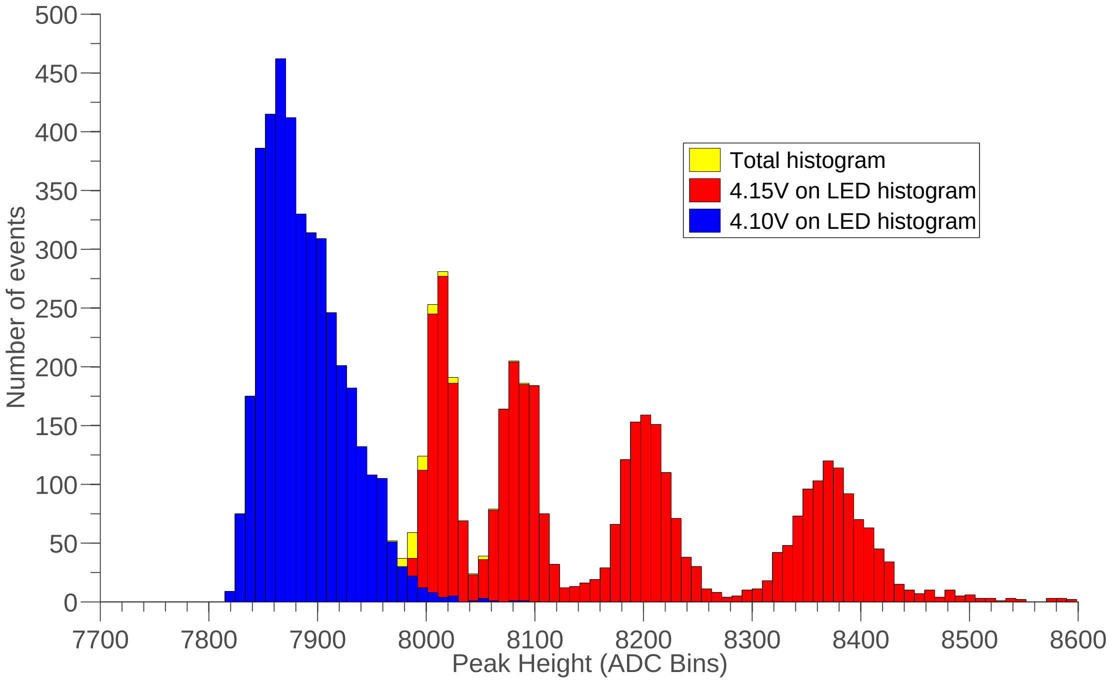

FIGURE 4.3: Histogram of the data of Figure 4.2.

4.3 Minimal APD Signal Detection

In a test to determine the minimal amount of photons emitted that can be reliably detected with the APDs, the voltage burst width on the LEDs is reduced to 100 ns.

While the LED is disabled, the background noise peak can be measured. Subtracting said histogram from that of a signal peak created by the light emitting LED shows clearly at what voltage a signal is detected. The acquisition software operates at a 8000 ADC bins baseline, hence the corresponding offset in positioning of the background peak.

At 4.50 V LED voltage, there is a peak in red, while in yellow the background noise peak is shown (See Figure 4.4). The red peak is the LED light emission converted into an APD signal. This observation is based on that peak increasing size rapidly for higher voltages, the general gaussian shape of the peak, and its relative distance to the noise peak.

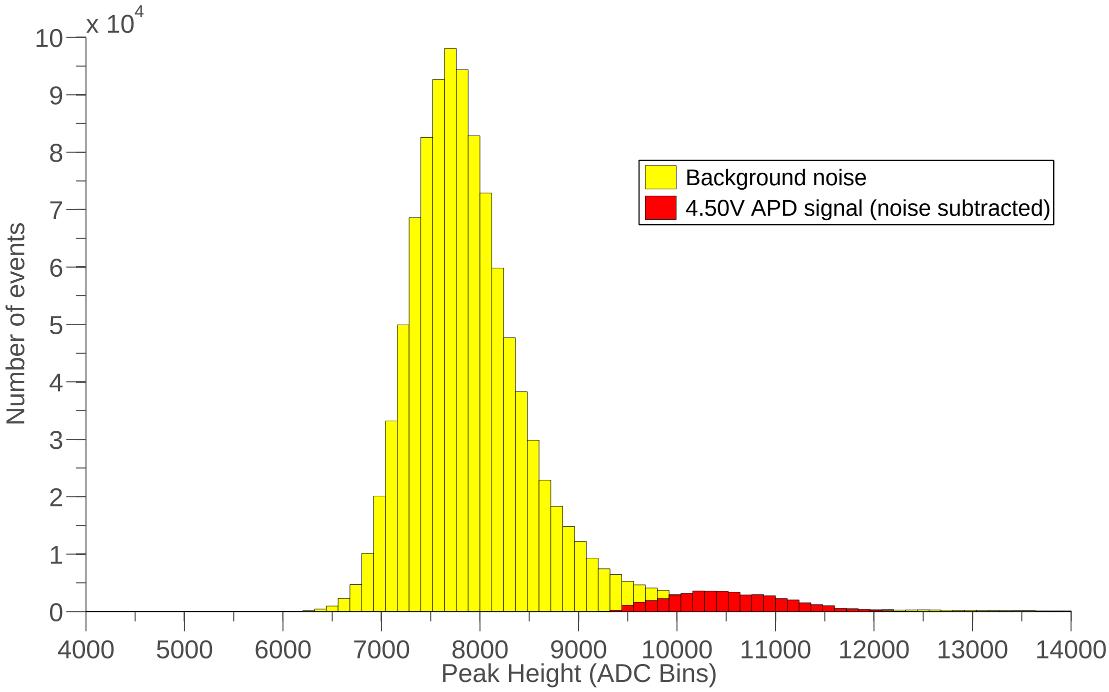

Figure 4.4: Minimal APD signal detection at 4.50 V. Histogram of signal with background (yellow) subtracted shows actual signal peak (red) at 10500 ADC bins.

At 4.45 V on the LED, the red peak disappears (See Figure 4.5). This is the point where not enough photons are emitted by the LED to create a substantial amount of photoelectrons in the APD. This factor is determined by the quantum efficiency of the APD. As a result, the photoelectron count that is too low leads to a signal that is not amplified enough, as not every single photoelectron is colliding with silicon crystal lattices and thus avalanching. For single photon counting, APDs would have to be operated in Geiger mode [18].

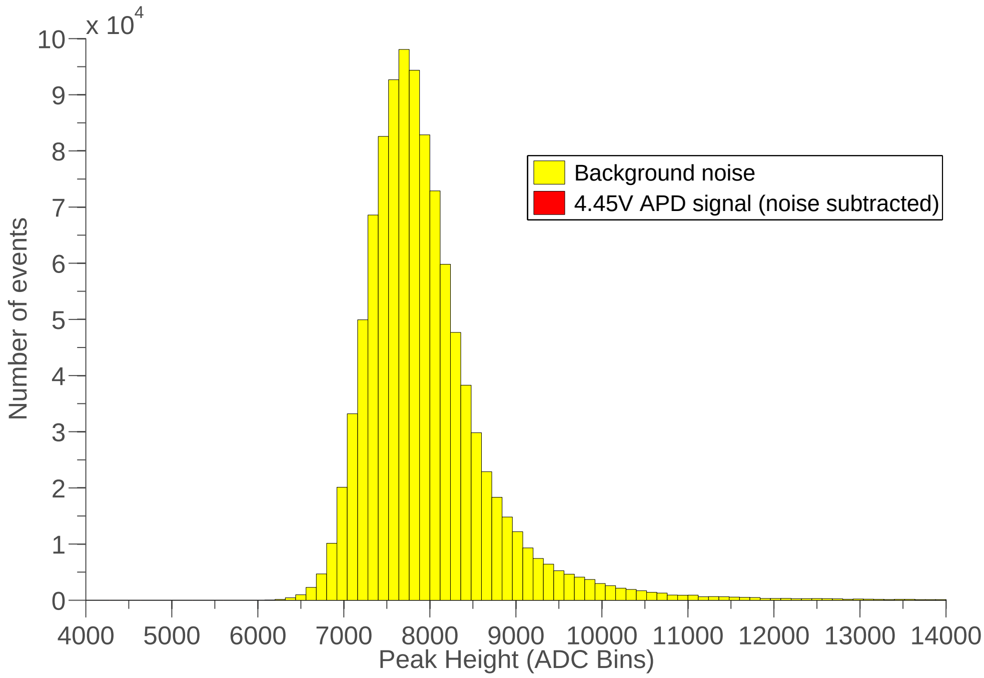

FIGURE 4.5: Minimal APD signal detection at 4.45 V. Histogram of signal with background (yellow) subtracted. The actual signal peak at 10500 ADC bins of Figure 4.4 has disappeared.

The reliability of the identification is determined by the significance of the signal peak. The distance from the signal peak to the noise peak is measured in the standard deviation σ of the background signal's gauss fit. At around 3 σ, the rightmost peak can be classified as a signal peak even as low as 4.50 V LED voltage at 100 ns pulse width.

4.4 APD Gain Curve

To accurately quantify the amplification of an APD signal, it is important to create an APD gain curve. While the high voltage is varied, the LED is kept at a constant 5.10 V. The resulting function follows a specific shape: It ascends from below a saddle point at first, then after going through said saddle point, it curves up into a large growth for high voltages [6, 7].

This saddle point is defining unity gain of the APD: The photoelectrons are not avalanching, but simply transported. The signal is not amplified.

For increased high voltages, the avalanching factor of the photoelectrons is following the APD gain curve's shape and is thus increasing rapidly. Below the saddle point, the

Parameter	Value	Parameter	Value
p_1	$2.57 \cdot 10^{-11}$	p_4	$-3.90 \cdot 10^{-2}$
p_2	$-6.27 \cdot 10^{-8}$	p_5	13.59
p_3	$6.86 \cdot 10^{-5}$	p_6	10813

TABLE 4.1: The parameters of Equation 4.1 corresponding to the polynomial fit of the low level APD gain curve of Figure 4.6.

recombination of primary electron-hole pairs is responsible for a drop in amplification below unity gain [7].

Normalising to unity gain allows the precise readout of signal amplification through avalanching inside the APD.

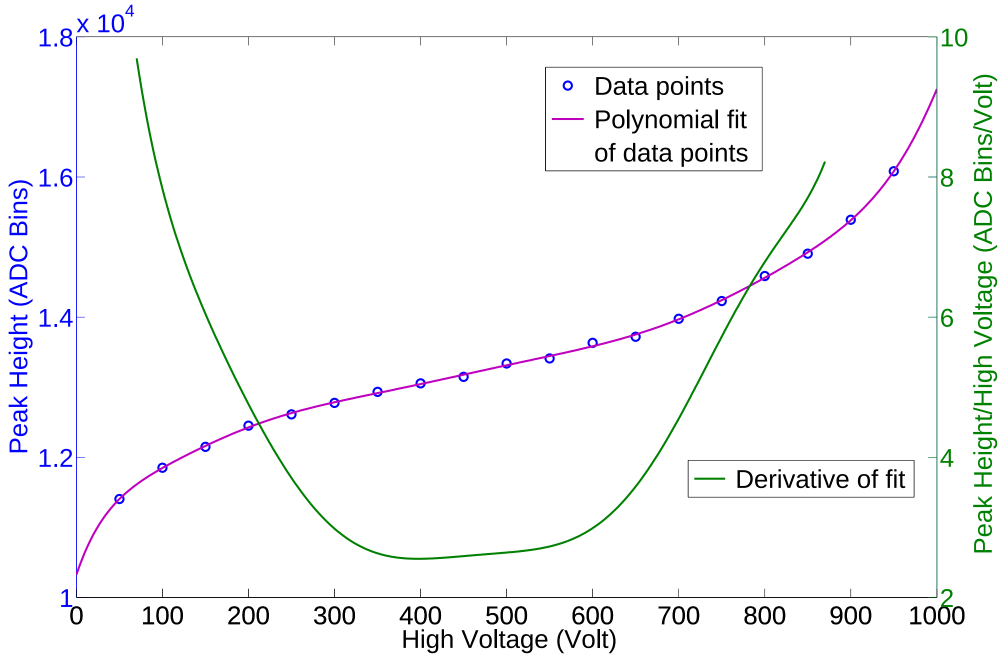

FIGURE 4.6: Low level APD gain curve ranging from 0 – 1000 V high voltage. At 400 V is the saddle point.

A low level gain curve in xenon gas is the first in a series of gain curve measurements (See Figure 4.6). The typical shape of the function can best be seen here for a non-logarithmic y-axis. The saddle point is located at 400 V. This is determined by taking the derivative of the polynomial fit (See Equation 4.1 and Table 4.1) of the data points.

$$y = p_1 \cdot x^5 + p_2 \cdot x^4 + p_3 \cdot x^3 + p_4 \cdot x^2 + p_5 \cdot x + p_6 \tag{4.1}$$

Looking at a gain curve over the full high voltage range in Figure 4.7, the very large amplification at higher voltages becomes apparent. The same voltage on the LED is used throughout the measurement. The graph is achieved through manually varying the

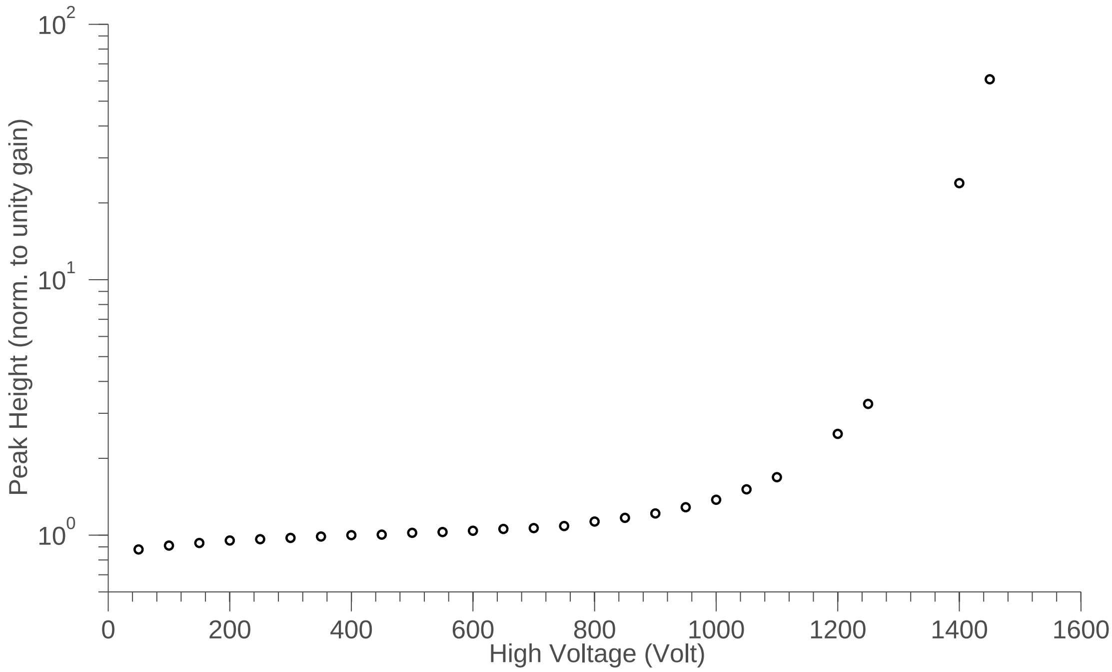

FIGURE 4.7: APD gain curve at 188 K temperature ranging from 0 – 1450 V high voltage. Maximum amplification of 60. Unity gain is located at exactly 400 V high voltage.

ORTEC 671 Amplifier gain from $\times 1000$ for low high voltages, down to $\times 5$ for the upper end to avoid saturation. Recalculation of the signal strength by the use of the amplifier calibrations shown in Chapter 4 produces the final graph.

Calculating the saddle point of the function reveals that it is located precisely at 400 V high voltage. Normalising all other data points to the unity gain at 400 V shows a maximum signal amplification factor of 60 for the highest achievable voltage (1450 V). This measurement is made at 188 K: The xenon is still in gas form.

With the temperature control system (See Section 3.3) in place, the xenon can be kept stable at 170 K. This is where the xenon becomes liquid (See Figure 3.10).

As can be seen in Figure 4.8, at 170 K the high voltage can be increased beyond the point of the 188 K measurement without a problem, so a maximum of 1567 V is achieved. This leads to a much higher amplification by the APD reaching a large APD gain factor of $2.37 \cdot 10^4$.

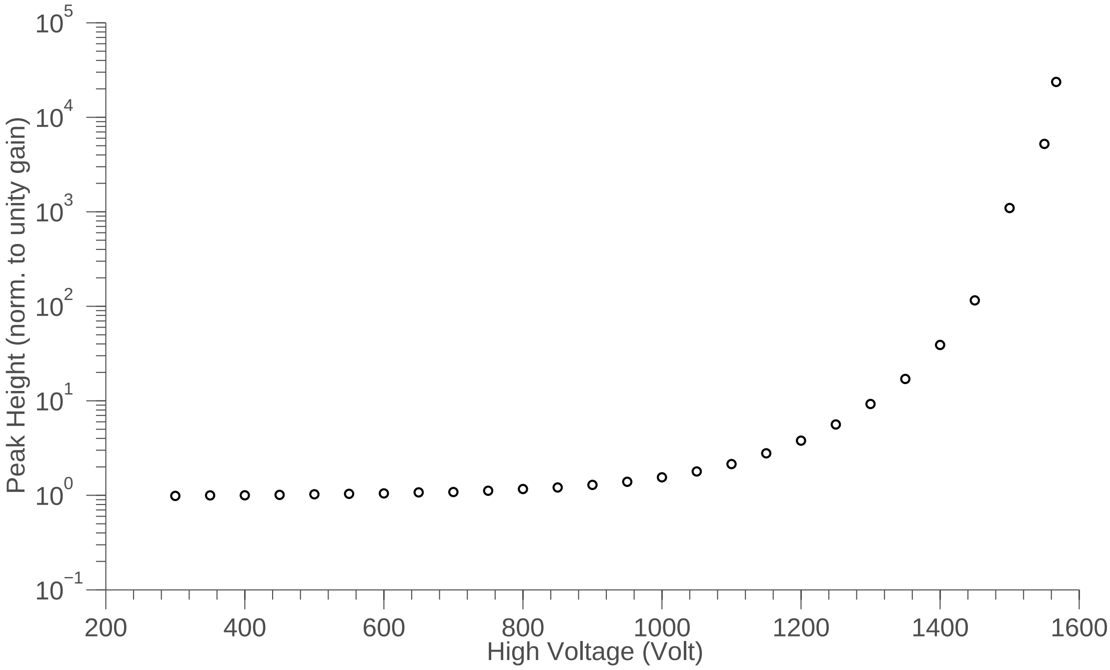

FIGURE 4.8: APD gain curve at 170 K temperature ranging from 0 – 1567 V high voltage. Maximum amplification of $2.37 \cdot 10^4$.

4.5 MCA Analysis of APD Signal

Further measurements at 170 K explore the behaviour of signal in preparation for scintillation light detection. An MCA is used to build the individual histograms, each peak is measured separately and then normalised to events per second. As opposed to an ADC, the MCA not only converts the analogue waveform into a digital one, but saves just its peak value. This is very useful when dealing with higher event rates.

At a fixed APD gain of $\times 1000$ at 1500 V, the LED voltage is increased (See Figure 4.9). The voltage burst width is at 200 microseconds. The signal shifts to the right for higher voltages on the LED, as expected from the previous ADC measurements (See Section 4.2).

At 2.94 V, the signal visibly goes into saturation on the oscilloscope.

For higher voltages, the peaks keep on shifting to the right on the graph until they reach the overflow bin at 8000 MCA bins. More and more artifact peaks are introduced due to the saturation.

As seen in Figure 4.10, another way to look at the behaviour of APDs in regards to signal variation is to keep the LED voltage constant and vary the high voltage. The increase shifts the peaks to higher MCA bins. Very noticeably, the peaks become broader and

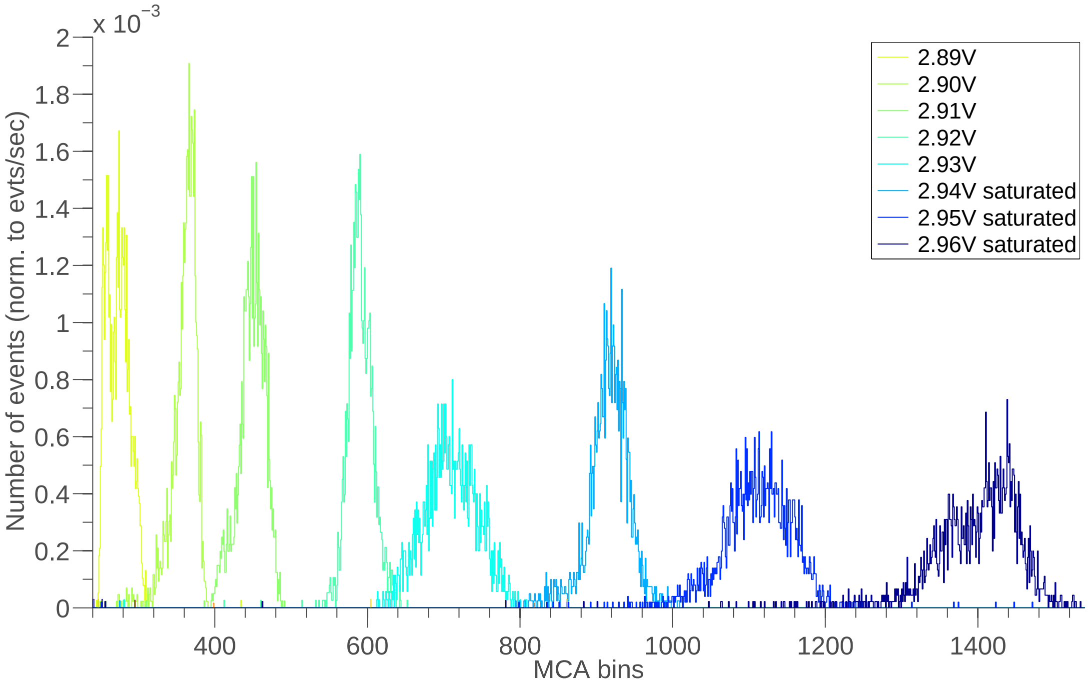

FIGURE 4.9: MCA measurement at fixed APD gain of ×1000 at 1500 V. Signal shifts to the right for higher LED Voltages.

broader the farther to the right they are. For lower voltages, the peaks are very narrow and precisely located on only a few MCA bins.

This peak width increase can be visualised by comparing the σ of the gauss fits for each peak, as seen in Figure 4.11. The graph shows a monotonic and continuous widening in correlation to the high voltage increase.

Statistical noise in the form of excess noise (See Section 2.2), due to the increasing multiplication ratio at higher voltages, could be responsible for the visible broadening of the peaks towards higher APD gain.

Equation 2.2 is used for an excess noise fit of the data points with a literature value of $k = 0.04$ for the electron-to-hole ionisation ratio [22, 23]. The adjusted R^2 value of the fit is 0.96. This is good evidence that the excess noise is the main factor that causes the decline of the signal-to-noise ratio at higher APD gain.

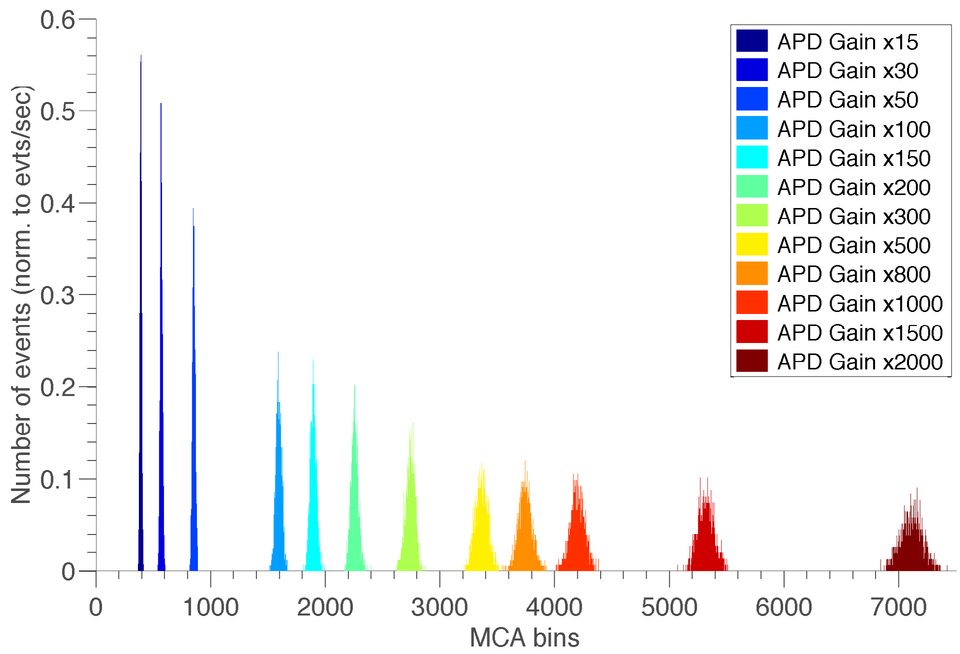

FIGURE 4.10: Varying the high voltage not only shifts the peaks, but also increases their width due to an increased excess noise factor. The respective APD gain values corresponding to the high voltage values are read out of Figure 4.8.

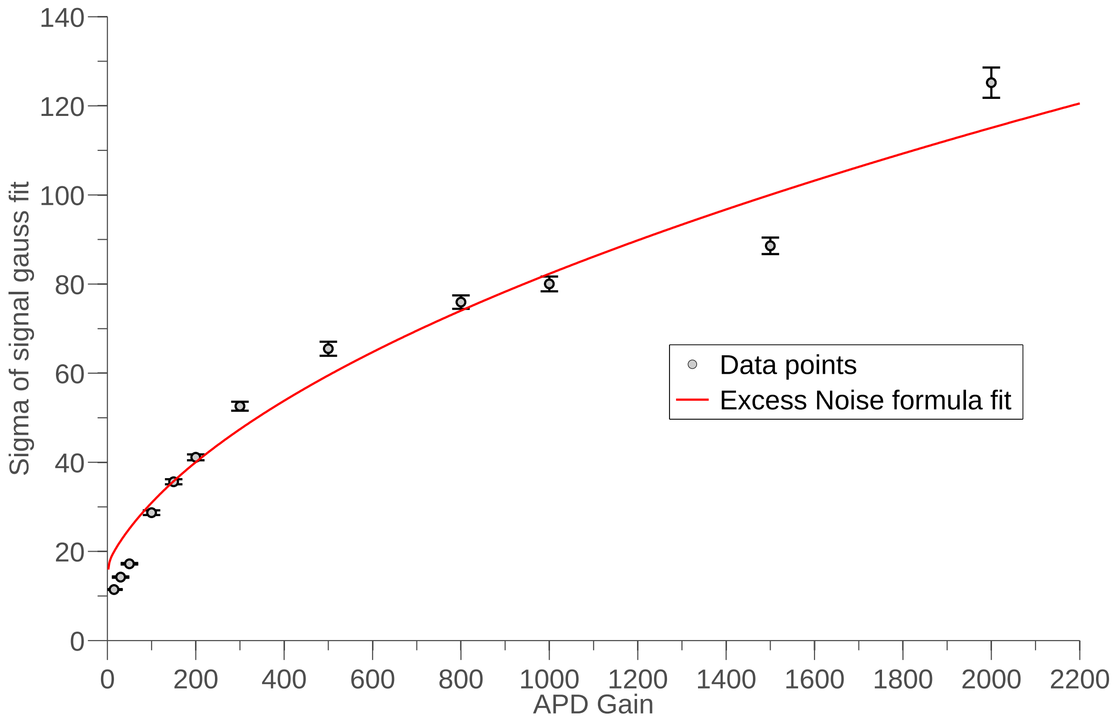

FIGURE 4.11: The σ-correlation curve of the gauss fits of Figure 4.10. Excess noise fit (red) using Equation 2.2 with $k = 0.04$ [22].

Chapter 5

Discussion

This chapter is about the interpretation of the measurement results followed by a direct comparison to existing literature.

The first paper, Ludhova et al. 2005 [7] performed at the Paul Scherrer Institute (PSI) in Switzerland, is interesting because of its detailed testing of an array of APDs for soft X-ray spectroscopy as a perspective for future large APD arrays used in high sensitivity detectors. Their operating temperature does not go below 223 K and is thus not in any direct relation to a liquid xenon detector.

This is where the second paper, Shagin et al. 2009 [6], differs. It tests a single APD in liquid xenon at Rice University (USA) to detect scintillation, measure APD quantum efficiency and APD gain.

5.1 Significance for Xenon Dark Matter Detectors

The signal comparison measurement between the two tested APDs in Section 4.1 shows a clear gain discrepancy between APDs of the same type. Using large arrays of APDs in high sensitivity detectors thus requires accurate gain matching.

The limit of sensitivity of APDs is studied in Section 4.3. Single photon counting in normal operating mode is not possible. In a liquid xenon detector chamber at S1, as seen in Figure 1.2, single photon counting is necessary for detecting the low quantity of photons emitted through the decay of excited molecular xenon states. At S2 however, where the free electrons move into the gas phase of the xenon and create a flash of light, the amount of photons is significantly higher. This allows for the conception of a hybrid detector: The top array detecting photon emissions from S2 consists of APDs in normal operation mode. With their small mass and high gain, they can do the job without introducing additional background radiation. The bottom array, close to S1, can be made up of either PMTs or APDs operated in Geiger mode, as both allow single photon counting.

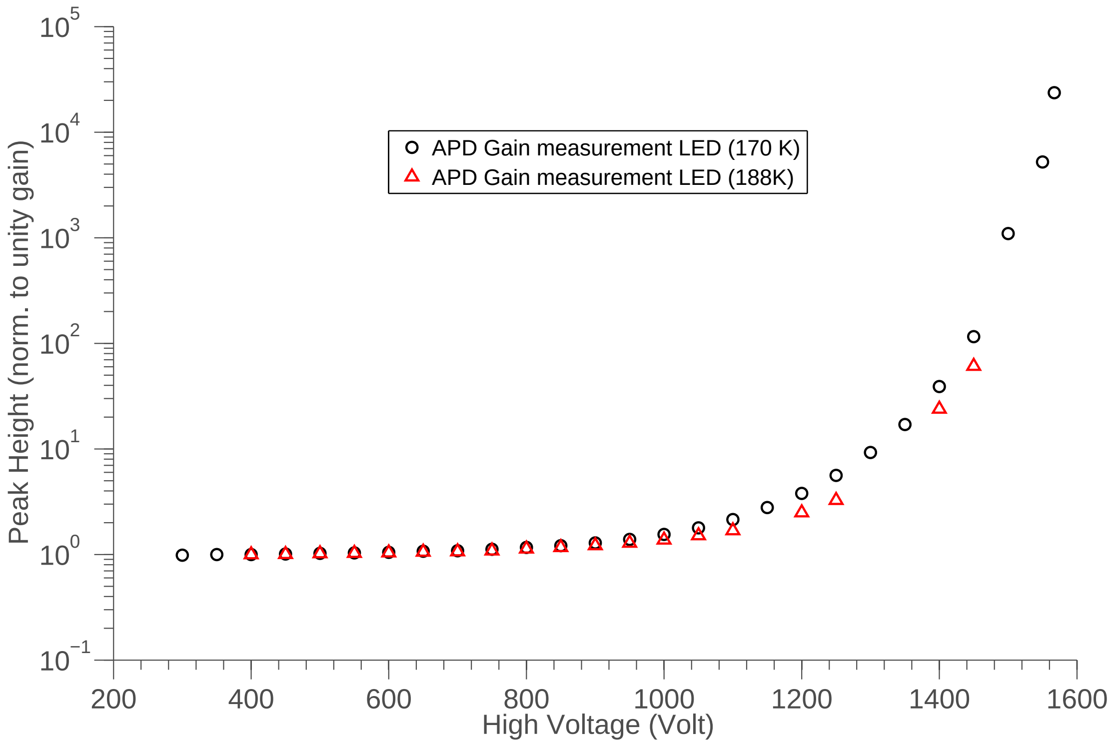

FIGURE 5.1: A comparison of Figure 4.7 showing the APD gain curve maximum of 60 at 188 K (red squares) and Figure 4.8 with maximum amplification of $2.37 \cdot 10^4$ at 170 K (black circles).

The APD gain curve measurements from 188 K and 170 K of Section 4.4 can be compared in Figure 5.1. The maximal achievable gain at 188 K is 60, when at 170 K the gain reaches up to $2.37 \cdot 10^4$. Even for equal high voltage, we see a drastic increase of gain at the lower temperature: At 1400 V the gain is 23 and 38 respectively, at 1450 V and 188 K it is 60, for 170 K even double that gain amount. The low temperature condition turns out to be beneficial to the usage of the APDs as they can be operated at lower high voltages to achieve the same amount of amplification.

The measurements in Section 4.5 show that excess noise increases for higher APD gain following the function outlined in Figure 4.11. For usage inside of a detector, a compromise needs to be made between higher APD gain for higher amplification and a lower APD gain for less excess noise and a better signal-to-noise ratio. An optimal point can be found during the detector calibration when there is sufficient amplification for the detection of photon emissions coming from S2 (See Figure 1.2).

5.2 Comparison with Ludhova et al. 2005 [7]

The goal of the experiment by Ludhova et al. is to measure the 2S Lamb Shift in muonic hydrogen. Two face-to-face rows of ten APDs are mounted inside a thermally insulated box. These 20 APDs are of identical type (RMD LAAPD S1315) to this experiment.

Similar to the findings seen in Section 4.1, where two APDs in this experiment are seen to have slightly different gains, the 20 APDs of Ludhova et al. show gains and resolution discrepancies as well. The latter are varying between 11% to 20% with an average of 15%. APDs thus require APD gain matching to work as an array.

In order to find the optimal operation temperature, various tests at different temperatures are made. The Ludhova et al. experiment is only concerned with achieving optimal operation temperature *without* any predetermined temperature obligations (such as liquifying xenon), aside from practicality. Their results reflect the temperature dependence of APD gain over a range of 280–223 K. Similar to this experiment (See Section 3.3), the temperature during each measurement was controlled to keep variations to a minimum.

The trend towards lower temperatures is most interesting for a direct comparison. They report that APD gain was measured to increase exponentially with lower temperature. The lower the temperature, the better the amplification. This is in accordance to the findings of Section 5.1 in Figure 5.1 where it is shown that the maximal achievable gain at 188 K is 60, when at 170 K the gain reaches up to $2.37 \cdot 10^4$ and that for equal high voltages the gain is much higher for lower temperatures.

Comparing the results of the APD gain measurements of the two experiments in Figure 5.2, we see the same shape of the curve with a dipping down below unity gain (Best seen in Figure 4.7) in the 300 V to 500 V region, a saddle point at unity gain, and large growth for higher voltages. The Ludhova et al. APD gain measurement using a red light LED was taken at 280 K, so the individually observed trend of more amplification at lower temperatures in mind, it is not surprising that in comparison the APD gain curves of Section 4.4 show much higher gain at equal voltages (See Figure 5.2). Excess noise factor measurements also show an increase for higher APD gain in accordance with the findings in Section 4.5.

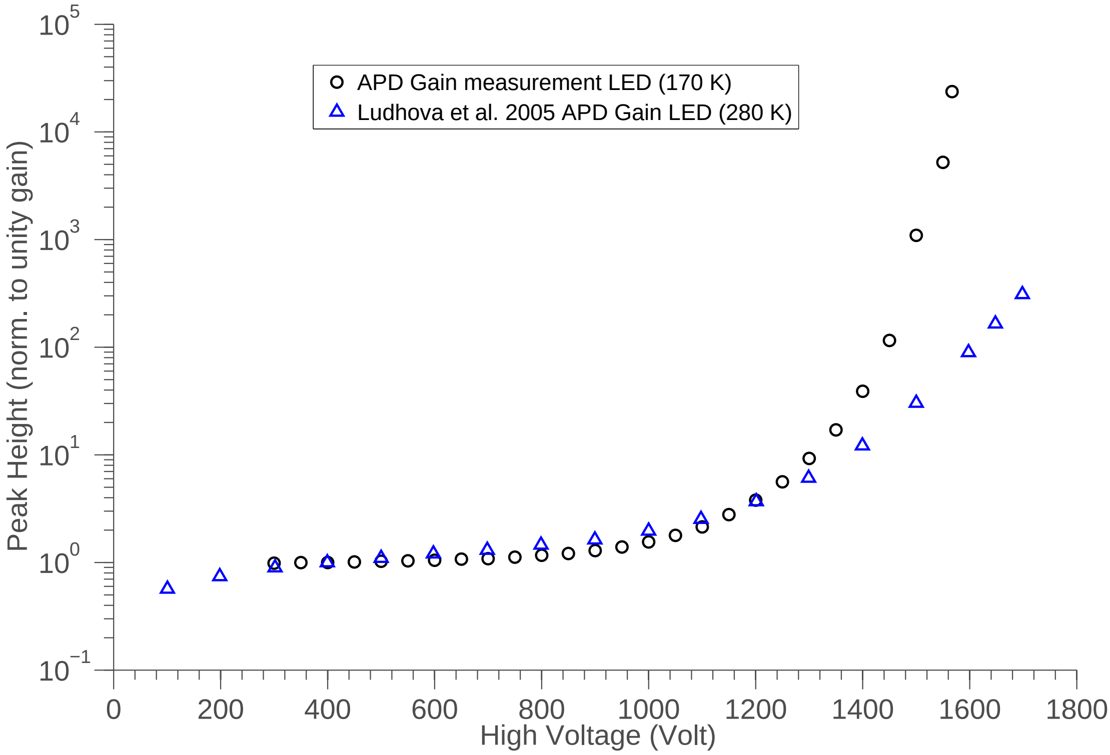

FIGURE 5.2: A comparison of the APD gain curve of Ludhova et al. 2005 [7] at 280 K with APD gain maximum at around 300 (blue triangles) and Figure 4.8 of this experiment with maximum amplification of $2.37 \cdot 10^4$ at 170 K (black circles).

5.3 Comparison with Shagin et al. 2009 [6]

The paper of Shagin et al. tests a single RMD LAAPD as a possible photodetector for liquid xenon scintillation light and is, as such, ideally suited as comparison literature.

Looking at Chapter 3, it can be seen that the setup of this experiment has been chosen to be similar to that of Shagin et al. for the ability of closer comparison. A teflon holder construct holds the APD in place when immersed. The Canberra PreAMP Model 2004 is fed with the APD signal by Shagin et al., while the Canberra PreAMP Model 2006 serves that purpose in this experiment. Both use the Ortec 671 Amplifier, which has been calibrated for APD gain calculation in Section 3.2.

Shagin et al. used temperatures between 167–188 K, but experienced significant temperature variation during their experiment, which had to be corrected through recalculation of results. This experiment, as shown in Section 3.3, uses a temperature controlling system to keep the temperature constant for accurate measurements.

Shagin et al. state that in order to achieve identical gain, operating at lower temperatures uses an exponentially lower high voltage compared to higher temperatures. The

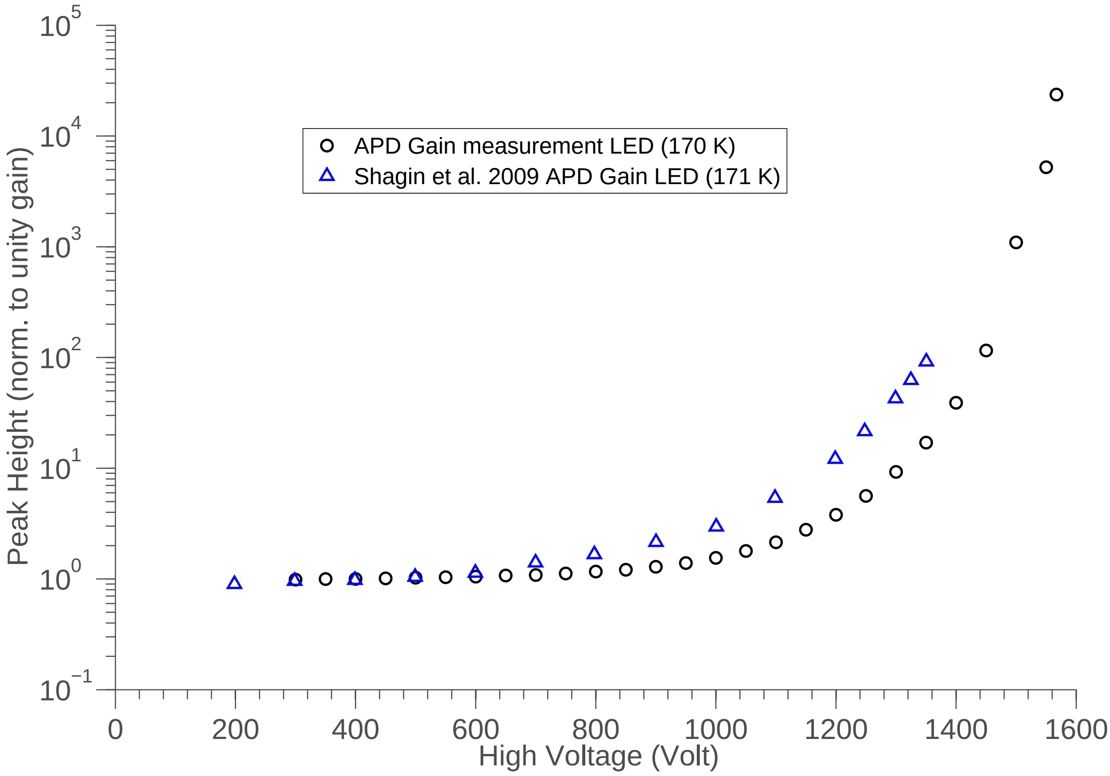

FIGURE 5.3: A comparison of the APD gain curve of Shagin et al. 2009 [6] at 171 K with APD gain maximum at around 10^2 for blue LED light (blue triangles) and Figure 4.8 of this experiment with maximum amplification of $2.37 \cdot 10^4$ at 170 K (black circles).

exponential increase of gain at lower temperatures found by Ludhova et al. for ideal operating conditions is thus not limited to the 223 K region, but down to at least 170 K. The earlier findings (See Figure 5.1) of better amplification at 170 K than at 188 K, when comparing the APD curves of Section 4.4, not only back this up, but show the specific trend working in favour of liquid xenon detection. The necessity of APDs having to be immersed in liquid xenon works out to be actually strongly improving the amplification ability of these photodetectors. The APD gain curve measured at 171 K of Shagin et al. shows the familiar shape and incidentally finds the saddle point and thus unity gain to be located at 400 V as well.

Differences in absolute APD gain for the same high voltage occurs between APDs, due to their silicon crystal nature (See Section 4.1). The shape comparison is important.

The measured APD gain of Shagin et al. peaks out at around 10^2 for blue LED light at around 1350 V high voltage. This experiment uses high voltages reaching up to 1567 V and thus not only matches these findings, but manages to achieve even higher amounts of APD gain to a maximum of $2.37 \cdot 10^4$ amplification.

Chapter 6

Conclusion and Outlook

The results of the measurements show that the APDs detect the light emitted by the LED not only in xenon gas from room temperature down to less than 188 K, but also in liquid xenon at 170 K.

In cross-reference with literature (See Chapter 5), the low temperature environment of liquid xenon is found to be vastly increasing the amplification capabilities of the APDs. The large gain of 10^4–10^5 make them an attractive photodetector alternative especially when considering the small size and associated radioactivity [6, 17, 18].

In use with high voltage almost every day for 4 months, they work as expected to the manufacturer's recommendations.

From here, the goal is to be able to detect liquid xenon scintillation light induced by a radioactive source. The MCA calibration (See Section 3.2) and behaviour analysis (See Section 4.5) are the first steps into that direction. Ludhova et al. 2009 [7] show promising results for 241-Am α-particle detection [7].

The quantum efficiency of the APDs, talked about in Section 4.3 on the topic of minimal APD signal detection, is also an aspect to be further explored. Measurements found in other literature have found convincing results [7, 24, 25].

APDs are an interesting avenue for use in high purity experiments and could soon have a future as large arrays inside next generation liquid xenon hybrid detectors used for Dark Matter detection.

Bibliography

[1] Planck Collaboration, P. A. R. Ade, N. Aghanim, C. Armitage-Caplan, M. Arnaud, M. Ashdown et al., *Planck 2013 results. I. Overview of products and scientific results*. ArXiv e-prints, Mar. 2013, `arXiv:1303.5062`.

[2] K. Jedamzik and M. Pospelov, *Big Bang nucleosynthesis and particle dark matter*. New Journal of Physics, 11(10):105028, Oct. 2009, `arXiv:0906.2087`.

[3] E. Aprile, M. Alfonsi, K. Arisaka, F. Arneodo, C. Balan, L. Baudis et al., *Dark Matter Results from 225 Live Days of XENON100 Data*. Physical Review Letters, 109(18):181301, Nov. 2012, `1207.5988`.

[4] Xenon100 Collaboration, E. Aprile, K. Arisaka, F. Arneodo, A. Askin, L. Baudis et al., *The XENON100 dark matter experiment*. Astroparticle Physics, 35:573–590, Apr. 2012, `arXiv:1107.2155`.

[5] E. Aprile, K. Arisaka, F. Arneodo, A. Askin, L. Baudis, A. Behrens et al., *Study of the electromagnetic background in the XENON100 experiment*. Physical Review D: Particles, Fields, Gravitation and Cosmology, 83(8):082001, Apr. 2011, `1101.3866`.

[6] P. Shagin, R. Gomez, U. Oberlack, P. Cushman, B. Sherwood, M. McClish et al., *Avalanche Photodiode for liquid xenon scintillation: quantum efficiency and gain*. Journal of Instrumentation, 4:1005, Jan. 2009.

[7] L. Ludhova, F. D. Amaro, A. Antognini, F. Biraben, J. M. R. Cardoso, C. A. N. Conde et al., *Planar LAAPDs: temperature dependence, performance, and application in low-energy X-ray spectroscopy*. Nuclear Instruments and Methods in Physics Research A, 540:169–179, Mar. 2005, `arXiv:physics/0410099`.

[8] F. Zwicky, *On the Masses of Nebulae and of Clusters of Nebulae*. The Astrophysical Journal, 86:217, Oct. 1937.

[9] V. C. Rubin, W. K. J. Ford, and N. . Thonnard, *Rotational properties of 21 SC galaxies with a large range of luminosities and radii, from NGC 4605 /R = 4kpc/ to UGC 2885 /R = 122 kpc/*. The Astrophysical Journal, 238:471–487, Jun. 1980.

[10] D. Clowe, M. Bradač, A. H. Gonzalez, M. Markevitch, S. W. Randall, C. Jones et al., *A Direct Empirical Proof of the Existence of Dark Matter*. The Astrophysical Journal, Letters, 648:L109–L113, Sep. 2006, `arXiv:astro-ph/0608407`.

[11] M. Weber and W. de Boer, *Determination of the local dark matter density in our Galaxy*. Astronomy & Astrophysics, 509:A25, Jan. 2010, `0910.4272`.

[12] Chandra X-ray Observatory Website, *Images of 1E 0657-56*. 1E 0657-56 with Scale Bar, 2006, URL `http://chandra.harvard.edu/photo/2006/1e0657/1e0657_scale.jpg`.

[13] M. Schumann, *Dark Matter Search with Liquid Noble Gases*. ArXiv e-prints, Jun. 2012, `1206.2169`.

[14] E. Aprile and XENON1T collaboration, *The XENON1T Dark Matter Search Experiment*. ArXiv e-prints, Jun. 2012, `1206.6288`.

[15] D. Mayani, *XENON TPC chamber Poster*. Invisibles School and Workshop, Jul. 2013.

[16] D. G. Phillips, II, E. Aguayo, F. T. Avignone, III, H. O. Back, A. S. Barabash, M. Bergevin et al., *The MAJORANA experiment: an ultra-low background search for neutrinoless double-beta decay*. Journal of Physics Conference Series, 381(1):012044, Sep. 2012, `1111.5578`.

[17] Hamamatsu Photonics, *Characteristics and use of Si APD (Avalanche Photodiode) SD-28*. KAPD9001E03, 2004, URL `http://www.hamamatsu.com/resources/pdf/ssd/si_apd_techinfo_e.pdf`.

[18] Hamamatsu Photonics, *Si Photodiodes*. Opto-Semiconductor Handbook, 22–66, 2013, URL `http://www.hamamatsu.com/resources/pdf/ssd/e02_handbook_si_photodiode.pdf`.

[19] C. Silva, J. Pinto da Cunha, A. Pereira, V. Chepel, M. I. Lopes, V. Solovov et al., *Reflectance of polytetrafluoroethylene for xenon scintillation light*. Journal of Applied Physics, 107(6), Mar. 2010, `arXiv:0910.1056`.

[20] E. Aprile and T. Doke, *Liquid xenon detectors for particle physics and astrophysics*. Reviews of Modern Physics, 82:2053–2097, Jul. 2010, `0910.4956`.

[21] G. D. Watkins, *Native Defects and their Interactions with Impurities in Silicon*. MRS Proceedings, 469, 1 1997.

[22] H. Melchior, A. R. Hartman, D. P. Schinke, and T. E. Seidel, *Atlanta Fiber System Experiment: Planar Epitaxial Silicon Avalanche Photodiode*. Bell System

Technical Journal, 57(6):1791–1807, 1978, URL http://dx.doi.org/10.1002/j.1538-7305.1978.tb02127.x.

[23] R. Neilson, F. Leport, A. Pocar, K. S. Kumar, A. Odian, C. Y. Prescott et al., *Characterization of large area APDs for the EXO-200 detector*. Nuclear Instruments and Methods in Physics Research A, 608:68–75, Sep. 2009, 0906.2499.

[24] V. N. Solovov, A. Hitachi, V. Chepel, M. I. Lopes, R. F. Marques, and A. J. P. L. Policarpo, *Detection of scintillation light of liquid xenon with a LAAPD*. Nuclear Instruments and Methods in Physics Research A, 488:572–578, Aug. 2002, arXiv:physics/0203011.

[25] K. Ni, E. Aprile, D. Day, K. L. Giboni, J. A. M. Lopes, P. Majewski et al., *Performance of a large area avalanche photodiode in a liquid xenon ionization and scintillation chamber*. Nuclear Instruments and Methods in Physics Research A, 551:356–363, Oct. 2005, arXiv:physics/0502071.